Biofuel Purification in GME Zeolitic–Imidazolate Frameworks: From *Ab Initio* Calculations to Molecular Simulations

Kang Zhang, Krishna M. Gupta, Yifei Chen, and Jianwen Jiang

Dept. of Chemical and Biomolecular Engineering, National University of Singapore, Kent Ridge 117576, Singapore

A multiscale modeling study is reported on the adsorption of ethanol/water in five zeolitic–imidazolate frameworks (ZIFs) for biofuel purification. The ZIFs (ZIF-68, −69, −78, −79, and −81) have isoreticular Gmelinite topology but differ in organic linkers. The simulated adsorption isotherms of ethanol and water in ZIF-68 agree fairly well with experimental data. At a low pressure, ZIF-78 exhibits the highest uptake due to strong hydrogen-bonding between ─NO₂ groups and adsorbates. The heats of adsorption at infinite dilution largely follow the trend of binding energies estimated from ab initio calculations. At a high pressure, the uptake is governed primarily by free volume but also affected by hydrogen-bonding. Among the five ZIFs, ZIF-79 with hydrophobic ─CH₃ groups shows the highest adsorptive selectivity for ethanol/water mixtures. This study provides microscopic insights into the adsorption and separation of ethanol/water in ZIFs, and would facilitate the development of new ZIFs for biofuel purification. © 2015 American Institute of Chemical Engineers AIChE J, 61: 2763–2775, 2015

Keywords: biofuel, zeolitic–imidazolate frameworks, modeling, adsorption, separation

Introduction

It is a great pleasure to dedicate this manuscript to Professor John M. Prausnitz as a tribute to his tremendous and profound impact on molecular thermodynamics and chemical engineering science. I (JJ) was fortunate to have the privilege to work with him as a research fellow during 1998–1999. The time in Berkeley is always highly memorable. I enjoyed and treasured the technical or nontechnical meetings with John in 308 Gilman Hall, which were truly enriching and inspiring not only in science and engineering but also in art and music. From John, I benefited enormously on how to strike out for new ideas, identify right methods, find appropriate colleagues for consultation, improve writing skills, etc. After I left Berkeley and even when I am now in the Eastern Hemisphere, John always generously offers his strong support, valuable advice, and constant encouragement for my research and personal life. For all these, I am extremely grateful!

Since the industrial revolution, CO_2 concentration in the atmosphere has increased by 43% (from 280 to 400 ppm) due to the intensive combustion of fossil fuels. This has led to the rise of global surface temperature and detrimental effects on environment.[1] In the last decade, there has been considerable scientific and commercial interest worldwide to develop renewable energy resources such as biofuels.[2] With less emission of gaseous pollutants than fossil fuels, biofuels are environmentally more benign and carbon neutral. They can be produced from the largely available biological feedstock, and thus, have a great potential to replace fossil fuels.[3] It has been projected that biofuel production will double from 75 bn litres in 2010 to 160 bn litres in 2019.[4] Currently, most biofuels are produced through fermentation with a low concentration of alcohol in aqueous medium.[5,6] It is a prerequisite to separate alcohol/water mixtures to produce fuel-grade biofuels.

Distillation is a conventional technology for the separation of alcohol/water mixtures; however, it involves energy-intensive boiling and condensing processes.[7] In addition, azeotropic mixtures that are commonly formed by alcohol and water cannot be simply separated by distillation. In this context, adsorption in porous materials turns out to be an energy-efficient and cost-effective technology. Various materials such as activated carbons, polymeric resins, and zeolites have been tested for the separation of alcohol/water, whereas their adsorption capacity and/or selectivity are not satisfactory.[8,9]

In an adsorption process, the separation efficacy is governed primarily by adsorbent. An ideal adsorbent should possess large surface area and pore volume, as well as high capacity and selectivity. Emerged as a new class of porous materials, metal-organic frameworks (MOFs) have received tremendous interest over the past a few years.[10] They can be synthesized by the judicious selection of inorganic and organic building blocks, and further modified by postsynthetic method. The degree of diversity and multiplicity in MOF structures is substantially more extensive than any other porous materials. Consequently, MOFs have been considered versatile materials for storage, separation, catalysis, etc.[11] Nevertheless, most current studies for MOFs have

---

Additional Supporting Information may be found in the online version of this article.

Correspondence concerning this article should be addressed to J. Jiang at chejj@nus.edu.sg.

© 2015 American Institute of Chemical Engineers
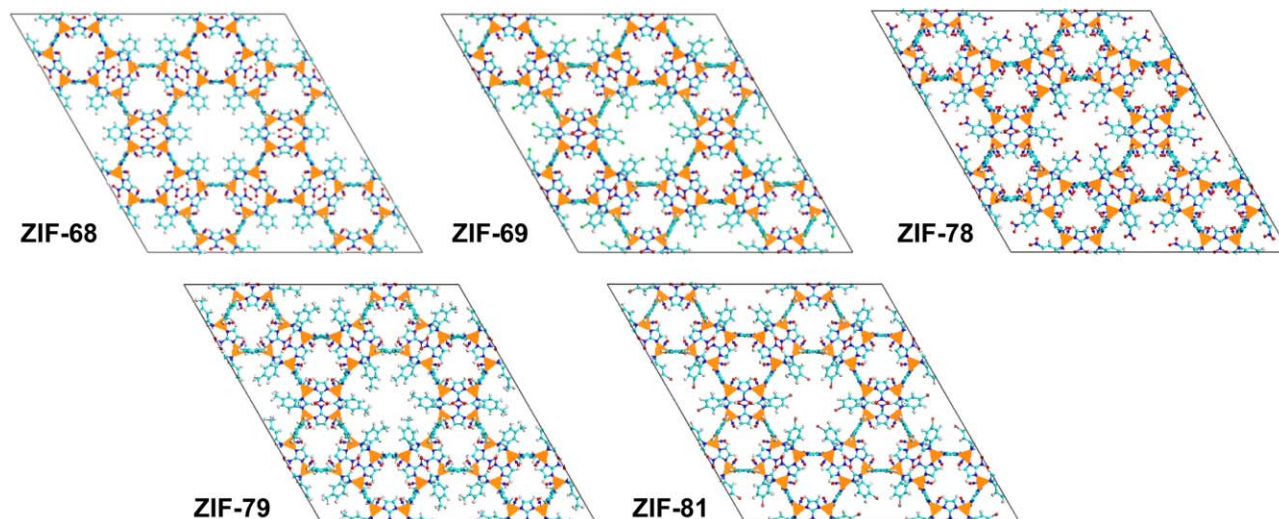
Figure 1. Atomic structures (2 × 2 unit cells) of ZIF-68, −69, −78, −79, and −81. ZnN₄: orange polyhedron, C: cyan, O: red, N: blue, Cl: green, Br: brown, H: white.

[Color figure can be viewed in the online issue, which is available at wileyonlinelibrary.com.]

been focused on the storage of low-carbon footprint energy carriers (e.g., H_2 and CH_4) and the separation of CO_2-containing gas mixtures.[12–14] There are only few studies examining MOFs for the separation of alcohol/water. For example, the adsorption isotherms of alcohol/water were experimentally measured in zeolitic–imidazolate framework (ZIF-8) and compared with those in carbon and silicalite.[15] Based on the adsorption of C_1—C_4 alcohols and water, the selectivity of alcohol/water was predicted in ZIF-8, ZIF-71, and ZIF-90.[16,17] The separation of ethanol/water was simulated in hydrophilic Na-*rho*-ZMOF and hydrophobic $Zn_4O(bdc)(bpz)_2$,[18] as well as in several ZIFs (ZIF-8, −25, −71, −90, −96, and −97) with various functional groups.[19] These simulation studies reveal that the hydrophobicity and functionality of MOFs play a crucial role in the separation of alcohol/water in MOFs.

In this study, we further investigate the adsorption of ethanol/water in five ZIFs (ZIF-68, −69, −78, −79, and −81) for biofuel purification. While this and previous study[19] are both focused on ZIFs, they differ largely in three aspects. First, two different topologies (Sodalite and Rho) were previously considered and they come into play together with functional groups. In contrast, the five ZIFs here possess isorecticular Gmelinite (GME) topology, thus, we can unambiguously elucidate the effects of organic linkers without the complex influence of topology. Second, multiscale modeling from *ab initio* calculations to molecular simulations is adopted in this study to fundamentally understand the microscopic interactions between adsorbates and ZIFs. Third, the mobility of adsorbates is also examined here in addition to equilibrium properties.

In Models section, the atomic models of ZIF-68, −69, −78, −79, and −81, as well as adsorbates are briefly described. The *ab initio* calculations and molecular simulations are outlined in Methods section, including Monte Carlo and molecular dynamics (MDs) techniques. In Results section, the adsorption isotherms, isosteric heats, radial distribution functions, density distributions, hydrogen-bonds, and mean-squared displacements (MSDs) of ethanol and water are presented; furthermore, the binding energies of ethanol and water with different organic linkers in the five ZIFs are

examined. Then, the adsorption isotherms and selectivities of ethanol/water mixtures are reported. The concluding remarks are summarized in Conclusions section.

Models

ZIFs are structurally similar to zeolites wherein the tetrahedral Si/Al nodes and O bridges are replaced by metal ions (usually Zn or Co) and imidazolate linkers, respectively. Figure 1 shows the atomic structures of ZIF-68, −69, −78, −79, and −81, all with the GME topology.[20,21] Each tetrahedral ZnN_4 cluster is connected to two 2-nitroimidazole (nIm) and two substituted benzimidazole (bIm) linkers. The five ZIFs consist of different substituted bIm linkers, which are bIm, 5-chlorobenzimidazole (cbIm), 5-nitrobenzimidazole (nbIM), 5-methylbenzimidazole (mbIm), and 5-bromobenzimidazole (brbIm) in ZIF-68, −69, −78, −79, and −81, respectively. Therefore, ZIF-69, −78, −79, and −81 can be considered as the functionalized counterparts of parent ZIF-68. As illustrated in Figure S1 of the Supporting Information, three types of cages exist in each ZIF, including small *hpr*, medium *gme*, and large *kno*. Six —NO_2 groups of nIm linkers point into the *hpr* cages, while the substituted bIm linkers reside inside the *kno* cages.

There are two types of one-dimensional (1-D) interconnected pores in the GME–ZIFs. The large pores comprise *kno* cages, while the small pores contain alternating *gme* and *hpr* cages. The large pores are nonpolar except ZIF-78, in which the —NO_2 groups of nbIm linkers are inside the *kno* cages, and thus, its large pores are polar; however, the small pores are less nonpolar. In a unit cell, one large and two small pores are present. Figure 2 shows the pore morphologies and diameters in ZIF-68 (see Supporting Information Figure S2 for ZIF-69, −78, −79, and −81). The diameters of cage (d_c) and aperture (d_a) were calculated from the HOLE program.[22] The accessible surface area, free volume, and porosity in each ZIF were calculated by in-house code. Specifically, N_2 with a kinetic diameter of 3.64 Å was used as a probe to estimate the accessible surface area S_a by rolling the probe over framework surface.[23] The free volume V_f
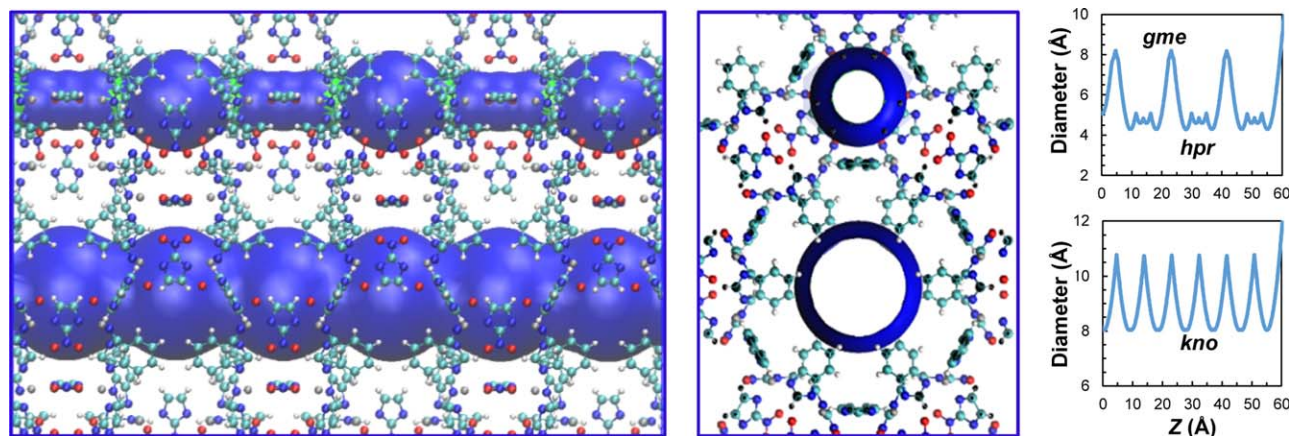
Figure 2. Pore morphologies and diameters in ZIF-68.

[Color figure can be viewed in the online issue, which is available at wileyonlinelibrary.com.]

was estimated by randomly inserting He, a nonadsorbing species, into framework.[24] The ratio of free volume over framework volume gave the porosity ϕ. Table 1 summarizes the structural characteristics of ZIF-68, −69, −78, −79, and −81. Due to the isoreticular topology, the five ZIFs have nearly identical dimensions (lattice constants). The estimated surface areas generally agree well with experimental data, particularly in ZIF-68 and −69. However, the values in ZIF-78, −79, and −81 are overestimated. The reason is that experimental samples might contain impurities, which would lead to smaller measured surface areas. Among the five ZIFs, ZIF-68 has the largest surface area, free volume, and porosity. This is because these quantities are reduced on substituting the bIm linker in ZIF-68 by bulkier linkers. Moreover, the pore diameters (both d_c and d_a) in ZIF-68 are the largest compared with the other four ZIFs. The aperture diameter d_a in the five ZIFs ranges from 3.6 to 4.3 Å. In principle, a guest molecule with size larger than d_a cannot enter into the pores. Nevertheless, ZIF structures are not completely rigid, as their apertures can fluctuate and hence allow larger molecules to enter. Indeed, it was experimentally reported that ZIF-68 can accommodate C_1—C_6 alcohols, C_6 alkane isomers, and aromatics with
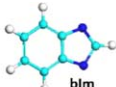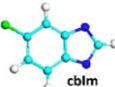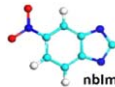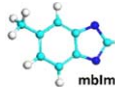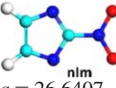
kinetic diameter substantially larger than its aperture size.[25,26] Similarly, this phenomenon also occurs in other ZIFs. For example, CH_4, 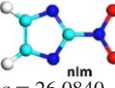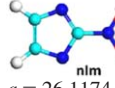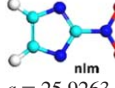C_2H_6, C_3H_8, and C_4H_{10} with kinetic diameter up to 5.0 Å are able to adsorb and diffuse in ZIF-8 with aperture size of 3.4 Å.[27,28]

The nonbonded interactions of ZIF atoms were represented by Lennard–Jones (LJ) and Coulombic potentials

$$U_{\text{nonbonded}} = \sum 4\varepsilon_{ij}\left[\left(\frac{\sigma_{ij}}{r_{ij}}\right)^{12} - \left(\frac{\sigma_{ij}}{r_{ij}}\right)^{6}\right] + \sum \frac{q_i q_j}{4\pi\varepsilon_0 r_{ij}} \quad (1)$$

where ε_{ij} and σ_{ij} are the well depth and collision diameter, r_{ij} is the distance between atoms i and j, q_i is the atomic charge of atom i, and $\varepsilon_0 = 8.8542 \times 10^{-12}$ C^2 N^{-1} m^{-2} is the permittivity of vacuum. In the literature, the DREIDING[29] and universal force field (UFF)[30] are commonly used to mimic the LJ potential in MOFs. In this study, three different force fields including DREIDING, UFF, and AMBER[31] were examined for ethanol and water adsorption in ZIF-68, and the one with the best matching with experimental data was used for the other four ZIFs. Supporting Information Table S1 lists the LJ parameters of ZIF atoms based on these three

Table 1. Structural Characteristics of ZIF-68, −69, −78, −79, and −81 [Color figure can be viewed in the online issue, which is available at wileyonlinelibrary.com.]

		ZIF-68	ZIF-69	ZIF-78	ZIF-79	ZIF-81
Organic linker		bIm / nIm	cbIm / nIm	nbIm / nIm	mbIm / nIm	brbIm / nIm
Dimensions (Å)		$a = 26.6407$	$a = 26.0840$	$a = 26.1174$	$a = 25.9263$	$a = 25.9929$
		$b = 26.6407$	$b = 26.0840$	$b = 26.1174$	$b = 25.9263$	$b = 26.4422$
		$c = 18.4882$	$c = 19.4082$	$c = 19.4910$	$c = 19.6532$	$c = 18.9703$
ρ (g cm^{-3})		1.032 (1.047)	1.146 (1.295)	1.175 (1.198)	1.074 (1.075)	1.291 (1.302)
S_a (m^2 g^{-1})		1083.56 (1090)	950.38 (950)	790.01 (620)	880.88 (810)	875.48 (760)
V_f (cm^3 g^{-1})		0.458	0.387	0.360	0.375	0.339
ϕ		0.473	0.444	0.423	0.403	0.438
hpr	d_a (Å)	4.3	3.7	3.6	3.7	3.6
	d_c (Å)	4.6	4.0	4.0	4.1	4.0
gme	d_a (Å)	4.3	3.7	3.6	3.7	3.6
	d_c (Å)	8.2	8.1	4.7	6.0	7.4
kno	d_a (Å)	8.0 (7.5)	5.8 (4.4)	4.5 (3.8)	5.6 (4.0)	4.7 (3.9)
	d_c (Å)	10.8 (10.3)	8.6 (7.8)	8.8 (7.1)	8.9 (7.5)	7.5 (7.4)

ρ: density, S_a: surface area, V_F: free volume, ϕ: porosity
Experimental data[20,21] are in parentheses.

force fields. The atomic charges of ZIFs were calculated by density functional theory (DFT) using GAUSSIAN 09.[32] As demonstrated in Supporting Information Figure S3, a fragmental cluster was adopted in the DFT calculation for each ZIF. The Becke exchange plus the Lee–Yang–Parr functional (B3LYP) was implemented, and the 6–31G(d) was used for all the atoms except Zn atoms for which the LANL2DZ basis set was used. By fitting to the electrostatic potentials using CHELPG scheme, the atomic charges were estimated as listed in Supporting Information Table S2.

Ethanol (EtOH) was represented by a united-atom model with each CH_x as a single interaction site. The potential parameters were adopted from the transferable potentials for phase equilibria (TraPPE) force field, which was fitted to the critical properties and vapor–liquid equilibria of hydrocarbons.[33] The bond lengths of EtOH were fixed, while the bending potential was described by

$$U_{\text{bending}} = \sum \frac{1}{2} k_\theta \left(\theta_{ijk} - \theta_{ijk}^0 \right)^2 \qquad (2)$$

where k_θ is force constant; θ_{ijk} is bond angle; and θ_{ijk}^0 is the equilibrium value. In addition, the torsional potential was described by

$$U_{\text{torsional}}(\phi) = c_0 + c_1[1+\cos\phi] + c_2[1-\cos(2\phi)] \\ + c_3[1+\cos(3\phi)] \qquad (3)$$

where c_i ($i = 0$, 1, 2, and 3) are force constants. Water (H_2O) was mimicked by the three-point transferable interaction potential model (TIP3P),[34] which gives reasonably good interaction energy compared with experimental value. Supporting Information Table S3 gives the potential parameters of EtOH and H_2O. The cross interaction parameters between ZIFs and adsorbates were estimated by the Lorentz-Berthelot combining rules.

Methods

Ab initio calculations

The five GME–ZIFs share the same nIm linker but differ in the substituted bIm linkers. To quantify the role of the substituted bIm linkers, their binding energies with a single EtOH or H_2O molecule were calculated by *ab initio* method using GAUSSIAN 09.[32] Specifically, the second Møller–Plesset perturbation method was adopted. First, the structures of a substituted bIm linker, an adsorbate molecule, and their complex were optimized separately at 6–31G basis set. Then, the single-point energy was calculated at a larger basis set of aug-cc-PVDZ. Finally, the binding energy was calculated by

$$\Delta E = E_{AB} - (E_A + E_B) \qquad (4)$$

where A or B represents a linker or an adsorbate, and AB refers to linker-adsorbate complex. The basis set superposition errors were corrected by the counterpoise method.[35]

Molecular simulations

The adsorption of pure EtOH and H_2O as well as their mixtures in ZIF-68, −69, −78, −79, and −81 was simulated by grand canonical Monte Carlo (GCMC) method.[36] The bulk phase was considered as a vapor for pure components, but a liquid for EtOH/H_2O mixtures to mimic biofuel. In EtOH/H_2O liquid mixtures, the fugacity of component i was estimated by

$$f_i = P_i^{\text{sat}} \phi_i^{\text{sat}} X_i \gamma_i \exp\left(\frac{\overline{V_i}(P - P_i^{\text{sat}})}{RT} \right) \qquad (5)$$

where P_i^{sat} is saturation pressure, ϕ_i^{sat} is fugacity coefficient, X_i is mole fraction in liquid phase, γ_i is activity coefficient, $\overline{V_i}$ is partial molar volume, P and T are operating pressure and temperature. ϕ_i^{sat} and the Poynting factor are approximately equal to unity under the conditions examined here.

In each ZIF, the simulation box contained 12 ($2 \times 2 \times 3$) unit cells and the periodic boundary conditions were exerted in 3-D. It has been demonstrated that structural flexibility has a negligible effect on alcohol adsorption in ZIFs,[37,38] thus, the ZIF structures were assumed to be rigid. A spherical cutoff of 15 Å was used to evaluate the LJ interactions with long-range corrections added. For the Coulombic interactions, the Ewald sum with a tin-foil boundary condition was used. The real/reciprocal space partition parameter and the cutoff for reciprocal lattice vectors were 0.2 Å^{-1} and 8, respectively, to ensure the convergence. Five types of trial moves were randomly attempted in the GCMC simulations, namely displacement, rotation, partial regrowth at a neighboring position, complete regrowth at a new position, and swap between reservoir including creation and deletion with equal probability. The total number of trial moves in a typical simulation was 4×10^7, in which the first half were used for equilibration and the second half for ensemble averages. In MC simulations of associating fluids such as EtOH and H_2O, it is important to improve sampling efficiency by unconventional method.[39] Here, the configurational-bias MC technique was adopted, in which adsorbate molecules were grown atom-by-atom biasing toward energetically favorable configurations while avoiding overlap with other atoms.[36] For pure EtOH or H_2O, 15 and 10 trial positions were generated for the first and subsequent atoms, respectively, with a probability proportional to $\exp(-\beta U_{\text{intra}}^i)$, where $\beta = 1/k_B T$ and U_{intra}^i is the intramolecular interaction energy at a position i. Then, one of the trial positions was chosen with a probability proportional to $\exp\left(-\beta U_{\text{inter}}^i\right) / \sum_i \exp\left(-\beta U_{\text{inter}}^i\right)$, where U_{inter}^i is the intermolecular interaction energy. For EtOH/H_2O mixtures, 20 and 15 trial positions were generated for the first and subsequent atoms, respectively. A modified version of BIGMAC[40] code was used for the GCMC simulations.

To estimate the mobility and hydrogen-bonds (H-bonds) of adsorbates in the ZIFs, MDs simulations were conducted using GROMACS v.4.5.[41] The mobility was quantified by MSD. An H-bond was counted if the donor and acceptor distance < 3.5 Å and the acceptor–donor–hydrogen angle $< 30°$. The initial configurations for MD simulations were taken from the final ones of the above GCMC simulations. Temperature was maintained by the Nosé–Hoover method with a relaxation time of 0.1 ps. The LJ interactions were evaluated with a cutoff of 12 Å, while the Coulombic interactions were calculated by the particle-mesh-Ewald technique with a grid spacing of 0.12 and a fourth-order interpolation. A linear constraint solver was used to constrain the bond lengths of EtOH and H_2O molecules. Each MD simulation duration was 12 ns, wherein the first 2 ns for equilibration and subsequent 10 ns for production. The potential and kinetic energies were monitored to ensure equilibration.

Results

First, the adsorption properties of pure EtOH and H_2O in ZIF-68, −69, −78, −79, and −81 are presented including
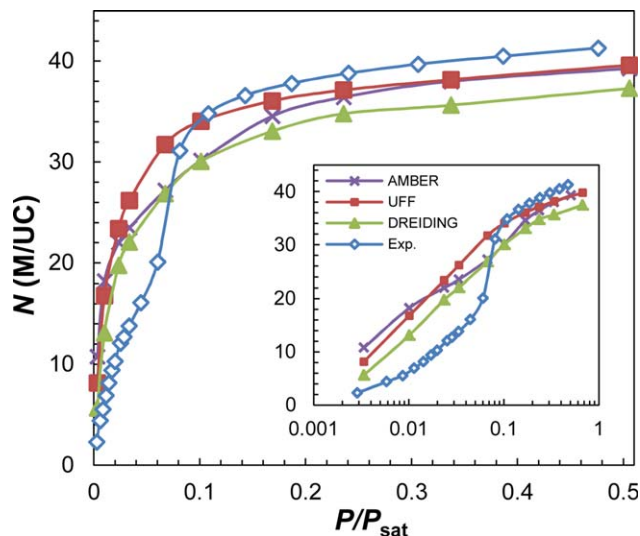
Figure 3. Adsorption isotherms of EtOH in ZIF-68 at 323 K.

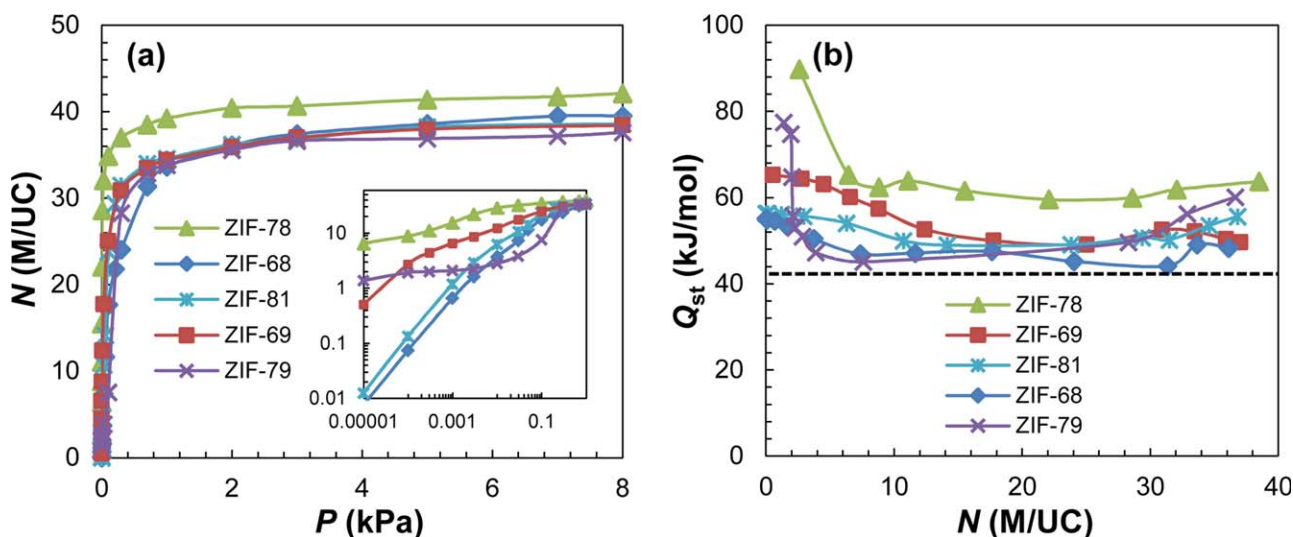[Color figure can be viewed in the online issue, which is available at wileyonlinelibrary.com.]

isotherms, isosteric heats, density distributions, radial distribution functions, H-bonds, and MSDs, as well as the binding energies with different organic linkers. From these comprehensive analyses, the effects of organic linkers are quantitatively evaluated. Then, the adsorptive separation of EtOH/H_2O mixtures is examined and the highest selectivity among the five ZIFs is identified.

Pure EtOH

Figure 3 shows the adsorption isotherms of EtOH in ZIF-68 at 323 K. The saturation pressure P_{sat} at 323 K is approximately 29.3 kPa.[42] In general, the predictions by the UFF, DREIDING, and AMBER match fairly well with the available experimental data.[25] While the measured values at low pressures are overestimated by the three force fields, the DREIDING gives the best matching. At high pressures, the saturation capacity is slightly underestimated. These devia-

tions might be due to two plausible factors: (a) the presence of structural defects or intercrystalline pores in experimental samples, thus, the measured extent of adsorption is smaller at low pressures but greater at high pressures compared with a perfect crystal as used in the simulation; (b) the three force fields are general for a wide range of systems but not specific for the ZIFs considered here, thus, a more accurate force field is desirable. Along with our previous study for the adsorption of C_1—C_4 alcohols in ZIF-8,[37] the DREIDING appears to outperform over the UFF, and AMBER for alcohol adsorption in ZIFs. Consequently, the DREIDING was further used for the simulations in the other four ZIFs (ZIF-69, −78, −79, and −81).

The simulated adsorption isotherms of EtOH in ZIF-68, −69, −78, −79, and −81 at 298 K are shown in Figure 4a. Over the entire pressure range, the isotherms belong to type I. Nevertheless, it should be noted that the experimental isotherm of EtOH in ZIF-68 appears to be sigmoidal.[25] Due to the plausible factors discussed above, the sigmoidal behavior is not observed in the simulation. All the five ZIFs possess favorable interactions with EtOH. At a low pressure, the uptake reflects the interaction strength of adsorbate-adsorbent. The uptake at 10^{-5} kPa decreases as ZIF-78 > -79 > -69 > -81 ~ −68, indicating that the EtOH-ZIF interaction is enhanced by functionalizing the bIm linker in ZIF-68. Particularly, the —NO_2 groups of nbIm linkers act as H-bonding sites and the greatest enhancement is seen in ZIF-78. This is consistent with a recent experimental study, which suggested that a large number of —NO_2 groups available in ZIF-78 could form H-bonds with cyclohexanol.[44] In ZIF-79, −69, and −81, although the —CH_3, —Cl, and —Br groups do not possess H-bonding capability, they offer additional adsorption sites and hence also enhance EtOH adsorption. At a high pressure (e.g., 8 kPa), the uptake decreases as ZIF-78 > -68 > -69 ~ −81 > -79, suggesting that the uptake near saturation is largely governed by free volume (or porosity). Specifically, the porosity in ZIF-68, −69, −81, and −79 is reduced from 0.473 from 0.403, which the trend of saturation uptake follows. The exception is ZIF-78 with a porosity of 0.423, smaller than that in ZIF-68, −69, and −81; however, the saturation uptake in ZIF-78 is the highest among the five ZIFs. This implies that

Figure 4. (a) Adsorption isotherms (b) isosteric heats of EtOH in ZIF-68, −69, −78, −79, and −81 at 298 K.

The dotted line indicates the heat of vaporization 42.3 kJ/mol.[43] [Color figure can be viewed in the online issue, which is available at wileyonlinelibrary.com.]
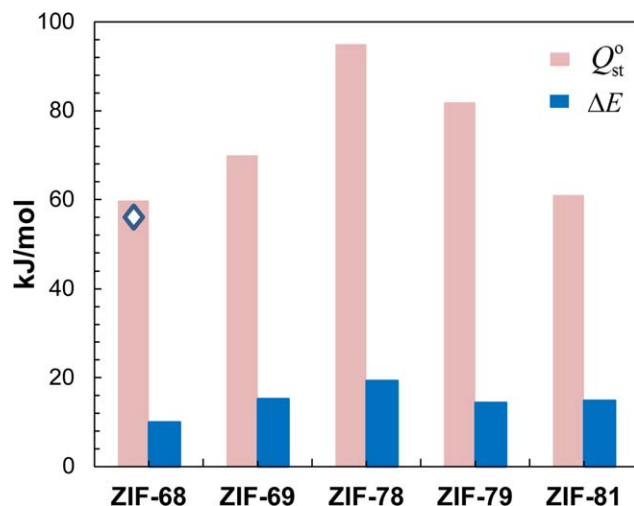
Figure 5. Binding energies between EtOH and substituted bIm linkers, and isosteric heats at infinite dilution of EtOH in ZIF-68, −69, −78, −79, and −81.

The $\diamond$ indicates experimental result.[26] [Color figure can be viewed in the online issue, which is available at wileyonlinelibrary.com.]

H-bonding also comes into play with porosity, particularly in ZIF-78, to determine the saturation uptake.

To quantify adsorption energy, the isosteric heat of adsorption Q_{st} was calculated by

$$Q_{st} = R_g T - \left(\frac{\partial U_{ad}}{\partial N_{ad}} \right)_{T,V} \qquad (6)$$

where R_g is gas constant, T is temperature, N_{ad} and U_{ad} are the number of adsorbates and adsorption energy, respectively. As plotted in Figure 4b, Q_{st} at a low loading follows ZIF-78 > -79 > -69 > -81 $\sim$ −68, which is consistent with the trend of uptake at a low pressure. With increasing EtOH loading, Q_{st} initially decreases, particularly in ZIF-78 and −79, then remains as constant and finally slightly increases. The initial decrease is attributed to the reduced number of favorable adsorption sites as loading increases. At an intermediate loading, EtOH molecules are dispersed in the pores, thus, nearly constant Q_{st} is observed. Nevertheless, EtOH molecules are closely packed at a high loading, thus, the cooperative interactions are strong, leading to an increase in Q_{st}. Over the entire pressure range, the Q_{st} is higher than the heat of vaporization because of the favorable framework-EtOH interaction, particularly in ZIF-78. Interestingly, the behavior of Q_{st} in the five GME–ZIFs at a low loading is remarkably different from that in ZIF-8. It was found previously that the Q_{st} of EtOH in ZIF-8 sharply increases at a low loading.[19] This is because no H-bonds are formed between EtOH and ZIF-8, but they start to form between EtOH molecules on adsorption. In contrast, the —NO$_2$ groups of nIm linkers can act as acceptors for H-bonding, thus, H-bonds can be formed between EtOH and each of the five GME–ZIFs.

Figure 5 shows the binding energies ΔE between EtOH and substituted bIm linkers estimated from *ab initio* calculations, the corresponding optimized structures are illustrated in Supporting Information Figure S5. Also shown are the isosteric heats at infinite dilution Q_{st}^o. Note that Q_{st}^o were esti-

mated by MC simulations for a single adsorbate molecule in a canonical ensemble.[37] The predicted Q_{st}^o in ZIF-68 is 59.8 kJ/mol, close to the experimental result (54.4 kJ/mol).[26] The ΔE ranges from −10 to −20 kJ/mol, much lower than Q_{st}^o. The reason is that only a single substituted bIm linker was used in *ab initio* calculations to estimate ΔE, while Q_{st}^o was predicted in a crystalline environment with multiple linkers. Therefore, the values of ΔE and Q_{st}^o should not be directly compared. More importantly, it is observed that ΔE decreases as ZIF-78 > -69 > -81 > -79 > -68, largely following the trend of Q_{st}^o (ZIF-78 > -79 > -69 > -81 $\sim$ −68). Among the five ZIFs, ZIF-78 has the greatest ΔE and Q_{st}^o, and vice versa for ZIF-68. The one out of the trend is ZIF-79, which has the fourth lowest ΔE but the second greatest Q_{st}^o. As we shall see below, EtOH molecules in ZIF-79 at a low loading reside solely in the small pores and do not interact with the mbIm linkers. This is due to the steric hindrance of bulky —CH$_3$ groups, but such effect was not taken into account in *ab initio* calculations. Consequently, it should be cautious that the binding energy between adsorbate and a building block may not necessarily reflect the actual interaction in a crystalline structure.

It is of central importance to elucidate the locations of adsorbed EtOH. Figure 6, thus, shows the simulated density contours of EtOH in ZIF-68, −69, −78, −79, and −81. At a low pressure (0.1 kPa), the small pores in all the five ZIFs are occupied by EtOH molecules; meanwhile, the six corners of large pores in ZIF-68, −69, −78, and −81 are also occupied. In remarkable contrast, however, the large pores in ZIF-79 are not accessible. The reason is that the mbIm linkers in ZIF-79 point toward the large pores and the bulky —CH$_3$ groups exert a steric hindrance, as mentioned above. The density in the large pores of ZIF-69, −78, and −81 is higher than that of ZIF-68, because the substituted bIm linkers enhance adsorption. In other words, the functional groups in ZIF-69, −78, and −81 act as extra adsorption sites. Particularly, the —NO$_2$ groups of nbIm linkers in ZIF-78 can form H-bonds with EtOH and lead to the greatest enhancement, as also seen in Figures 4 and 5. At a high pressure (8 kPa), pore filling occurs in the large pores of all the five ZIFs. The centre of large pores exhibits higher density except ZIF-78, in which the six corners proximal to —NO$_2$ groups are more densely occupied because of strong H-bonding.

To further quantitatively characterize adsorption sites, radial distribution functions of EtOH around the framework atoms were calculated by

$$g_{ij}(r) = \frac{N_{ij}(r, r+\Delta r)V}{4\pi r^2 \Delta r N_i N_j} \qquad (7)$$

where r is the distance between atoms i and j, $N_{ij}(r, r+\Delta r)$ is the number of atom j around i within a shell from r to $r + \Delta r$, V is the system volume, N_i and N_j are the numbers of atoms i and j, respectively. Figure 7 shows the $g(r)$ of EtOH around several typical ZIF atoms at 0.1 Pa. In all the five ZIFs, a pronounced peak at approximately 4 Å is observed around the C2 atoms of nIm linkers (see Supporting Information Figure S4 for notations), particularly in ZIF-68 and −79. This indicates the C=C bonds of nIm linkers are favorable for adsorption. In ZIF-79, the peak around the N1 atoms is also pronounced because of the exclusive location of EtOH in the small pores; as discussed in Figure 6, the large pores are not accessible at a low pressure due to
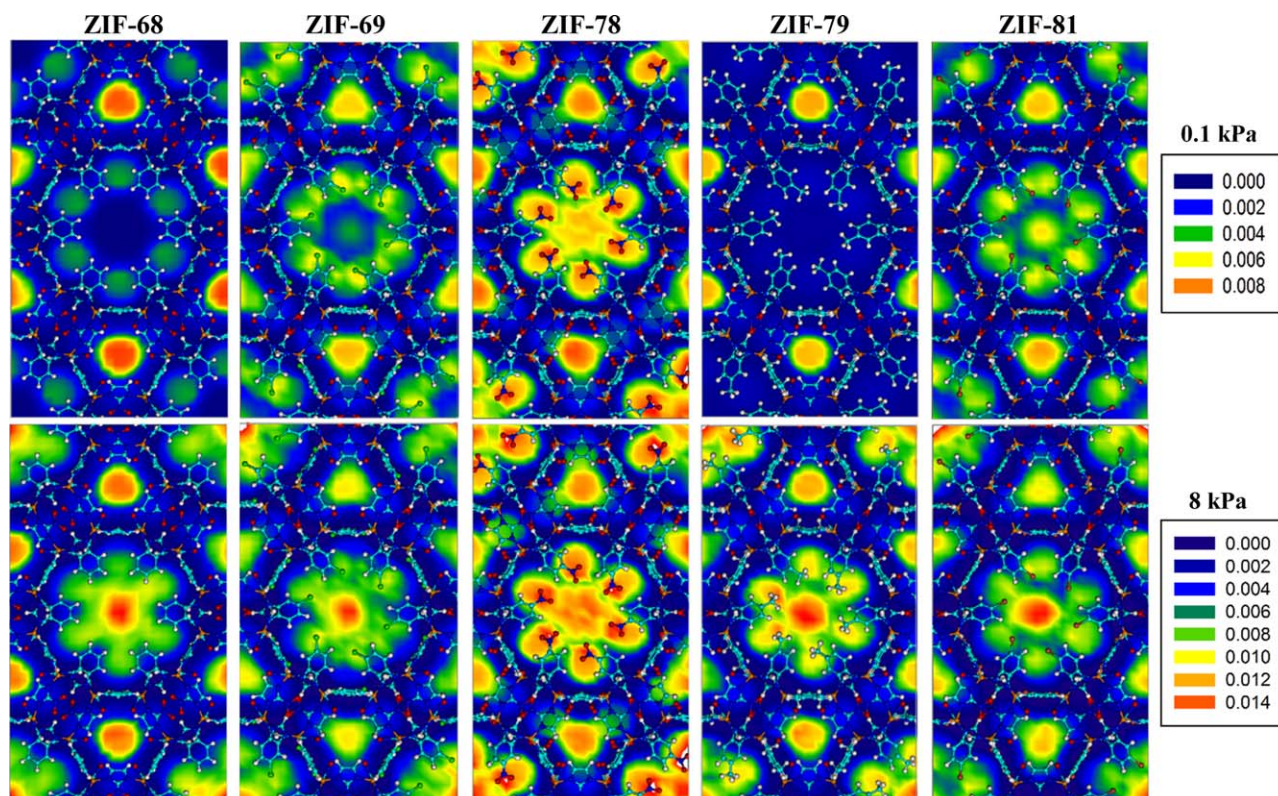
Figure 6. Density contours of EtOH at 0.1 and 8 kPa in ZIF-68, −69, −78, −79, and −81.

The unit of density scale is the number of molecules per Å³. [Color figure can be viewed in the online issue, which is available at wileyonlinelibrary.com.]

the steric hindrance of —CH₃ groups. Indeed, the peaks around the C2 and N1 atoms in ZIF-79 are higher than in the other four ZIFs. In ZIF-69 and −81, the bIm linkers are functionalized by —Cl and —Br as extra adsorption sites, and thus, peaks are seen at 4 Å around the Cl and Br atoms. In ZIF-78, a sharp peak is observed at 3 Å around the O atoms (—NO₂ groups) of nbIm linkers due to strong H-bonding. In all the five ZIFs, the $g(r)$ around the Zn atoms exhibit peaks at a long distance (5.5 Å), thus, the Zn atoms are less favorable.

H-bonding has a significant effect on EtOH adsorption in the GME–ZIFs. As shown in Figure 8a, the number of H-bonds formed between ZIF and EtOH increases with loading. Among the five ZIFs, the number decreases as ZIF-78 > -79 > -69 > -81 > -68, following the trend in Figure 4 at a low loading. In ZIF-78, the number is substantially greater than in the other four ZIFs. This is because the majority of EtOH molecules are located in the large pores rich with —NO₂ groups, thus, a large number of H-bonds are formed. Nevertheless,

—CH₃, —Cl, and —Br in ZIF-79, −69, and −81 have no capability of H-bonding. Thus, only a small number of H-bonds are formed with —NO₂ groups of nIm linkers in the small pores. This is also true in ZIF-68 with negligible amount of H-bonds, confirming ZIF-68 has the weakest affinity for EtOH among the five ZIFs. As shown in Figure 8b, the total number of H-bonds in each ZIF increases with loading. Unlike Figure 8a, however, the total number does not differ significantly among the five ZIFs, and it is indeed nearly identical in ZIF-78 and −79. The reason is that more H-bonds are formed between EtOH molecules compared with ZIF-EtOH.

It is instructive to examine the mobility of EtOH adsorbed in the ZIFs. To do so, MSD was calculated from MD simulation

$$\text{MSD}(t) = \frac{1}{KN} \sum_{k}^{K} \sum_{i=1}^{N} \left| \mathbf{r}_i(t + t_k) - \mathbf{r}_i(t_k) \right|^2 \tag{8}$$

where t is the time, N is the number of adsorbate molecules, and $r_i(t)$ is the position of ith molecule at time t. The
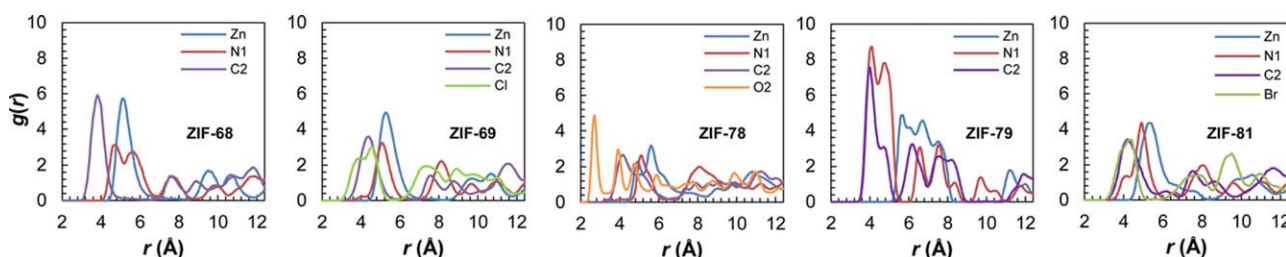
Figure 7. Radial distribution functions of EtOH around the framework atoms of ZIF-68, −69, −78, −79, and −81 at 298 K and 0.1 Pa.

[Color figure can be viewed in the online issue, which is available at wileyonlinelibrary.com.]
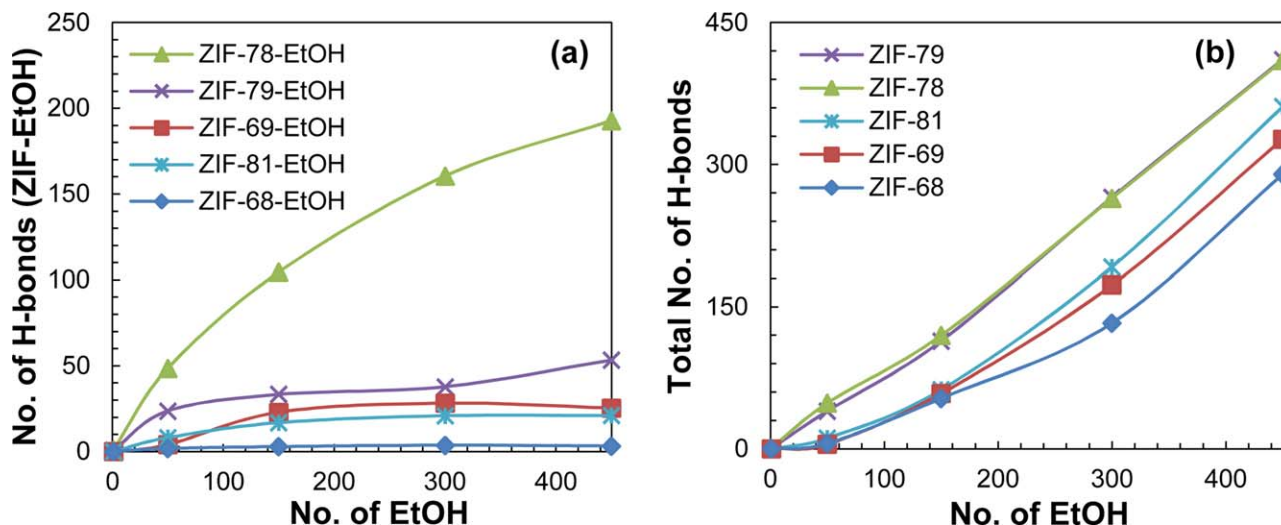
Figure 8. (a) Number of H-bonds formed between ZIF and EtOH (b) total number of H-bonds at 298 K.

The number of EtOH is based on 12 unit cells (the whole simulation box). [Color figure can be viewed in the online issue, which is available at wileyonlinelibrary.com.]

multiple time-origin method was used to evaluate MSD and K is the number of time origins. As shown in Figure 9, the MSD at a loading of 450 EtOH molecules in a simulation box with 12 unit cells (i.e., near saturation) increases as ZIF-79 < -78 < -81 < -69 < -68. In principle, a stronger ZIF-EtOH interaction would lead to lower mobility. Nevertheless, the hierarchy of MSD appears not to entirely follow the reverse trend of ZIF-EtOH interaction (ZIF-78 > -79 > -69 > -81 > -68, Figures 4 and 5). Near saturation condition here, it follows more closely the trend of porosity (ZIF-79 < -78 < -81 < -69 < -68). From a geometric point of view, EtOH in ZIF-68 has the highest MSD because of the largest porosity (free volume), while EtOH in ZIF-79 exhibiting the lowest MSD is attributed to the steric hindrance of bulky $-CH_3$ groups.

Pure H2O

Figure 10 shows the adsorption isotherms of H_2O in ZIF-68 at 303 K. The saturation pressure P_{sat} at 303 K is about

4.2 kPa.[42] The uptakes predicted by the UFF, DREIDING, and AMBER force fields are close to one another, and in good agreement with experimental data[25] at low pressure range ($P/P_{sat} < 0.2$). Moreover, the DREIDING appears to be slightly better compared with the UFF and AMBER. At $P/P_{sat} \approx 0.3$, capillary condensation is predicted by the three force fields, although not observed by experiment. From the trend of measured data, however, capillary condensation might be experimentally observable at high P/P_{sat}. Furthermore, it is worthwhile to note that the accuracy to simulate H_2O adsorption in MOFs strongly depends on the model of H_2O and the atomic charges of frameworks.[45–47] Therefore, more thorough modeling should be conducted for H_2O adsorption in MOFs.

The simulated adsorption isotherms of H_2O in ZIF-68, -69, -78, -79, and -81 at 298 K are plotted in Figure 11a. From the linear plot in Supporting Information Figure S6, the

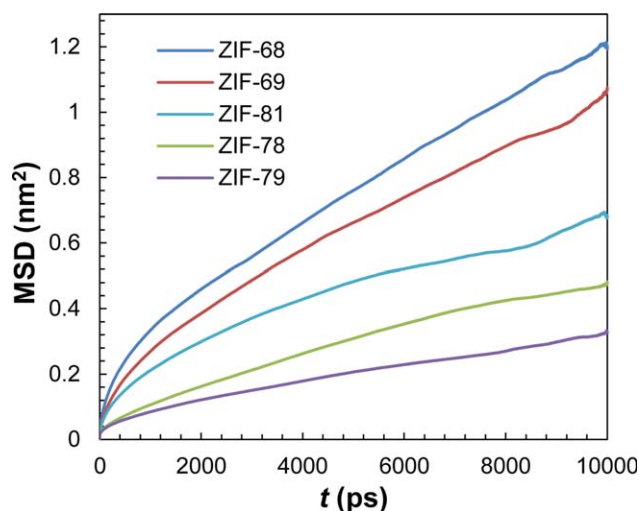**Figure 9.** MSDs of EtOH in ZIFs at 298 K.

[Color figure can be viewed in the online issue, which is available at wileyonlinelibrary.com.]

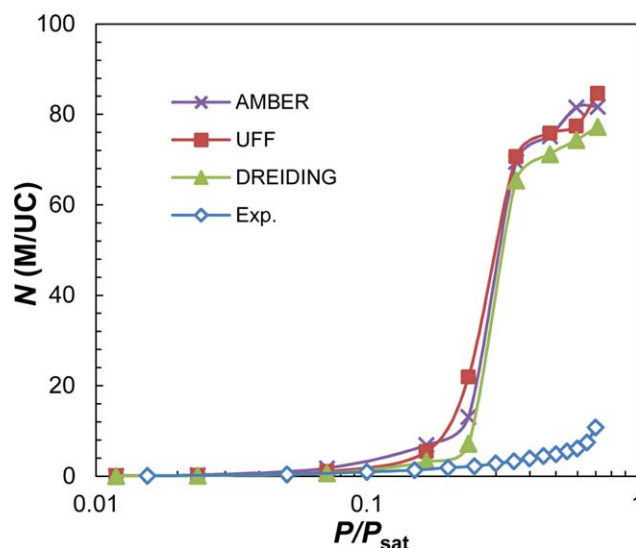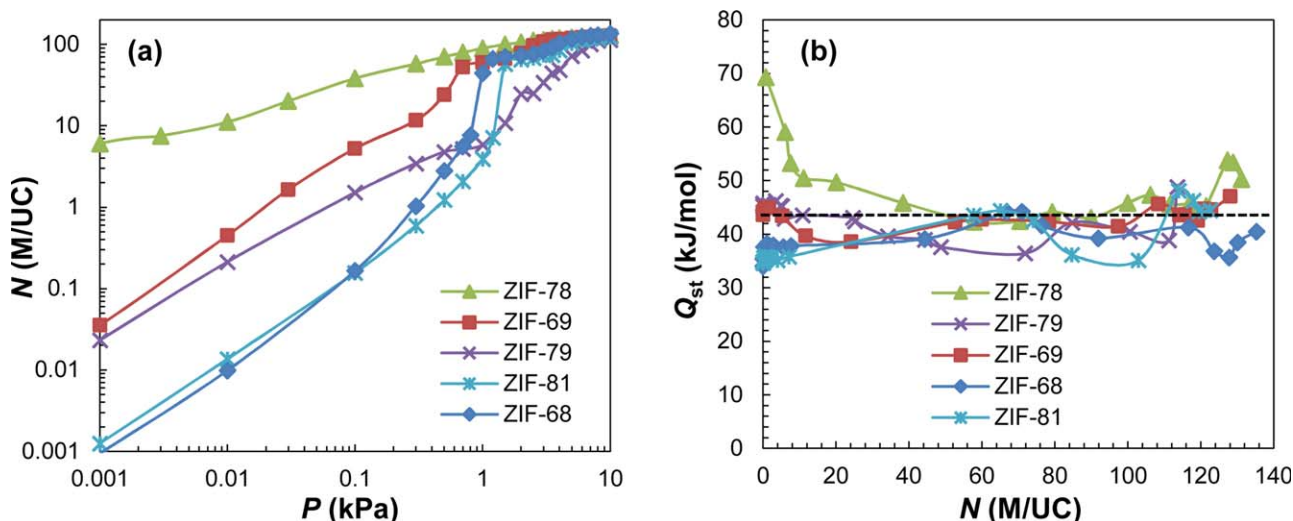**Figure 10.** Adsorption isotherms of H_2O in ZIF-68 at 303 K.

[Color figure can be viewed in the online issue, which is available at wileyonlinelibrary.com.]

Figure 11. (a) Adsorption isotherms (b) isosteric heats of H$_2$O in ZIF-68, −69, −78, −79, and −81 at 298 K.

The dotted line indicates the heat of vaporization 44.0 kJ/mol.[42] [Color figure can be viewed in the online issue, which is available at wileyonlinelibrary.com.]

isotherm is type I in ZIF-78 and type V in the other four ZIFs. On this basis, ZIF-78 can be classified as hydrophilic, and the other four tend to be hydrophobic. At a low pressure (e.g., 0.01 kPa), the uptake decreases in the order of ZIF-78 > -69 > -79 > -81 > -68. Apparently, the uptake in ZIF-78 is the highest as a result of H-bonding between H$_2$O and —NO$_2$ groups of nbIm linkers. Despite incapability of H-bonding, —Cl, —Br, and —CH$_3$ in ZIF-69, −81, and −79 act as additional adsorption sites, thus, the uptake in ZIF-69, −81, and −79 is higher than that in ZIF-68. At a high pressure (e.g., 8 kPa), the uptake follows ZIF-68 > -78 > -69 > -81 > -79. Similar to EtOH, the saturation capacity of H$_2$O is not simply dependent on free volume, instead, also governed by H-bonding. Despite the second smallest porosity, ZIF-78 contains —NO$_2$ groups of nbIm linkers and can strongly interact with H$_2$O via H-bonding, thus, exhibit the second highest uptake. Moreover, at an intermediate pressure (e.g., 4 kPa),

the uptake in ZIF-79 is substantially lower than in the other four ZIFs, and the underlying reason for this behavior will be discussed below when we visualize the density distributions of adsorbed H$_2$O molecules.

The isosteric heats Q_{st} of H$_2$O adsorption are plotted in Figure 11b. At a low loading, the Q_{st} decreases as ZIF-78 > -79 > -69 > -81 > -68, largely follows the trend of isotherm at a low pressure. With increasing loading, the Q_{st} decreases sharply in ZIF-78 because the preferential —NO$_2$ sites of nbIm linkers tend to be fully covered by H$_2$O and subsequent H$_2$O will interact with relatively weaker sites. For the same reason, the Q_{st} in ZIF-79 and −69 also decreases with loading, though in a smaller degree. On the contrary, the Q_{st} in ZIF-81 and −68 slightly increases as loading rises. This is because H-bonds are gradually formed among adsorbed H$_2$O molecules, while the interaction of H$_2$O with ZIF-68 and −81 is weak.

Figure 12 shows the binding energies ΔE between H$_2$O and substituted bIm linkers and the optimized structures are in Supporting Information Figure S7. The ΔE is in the range of $-8 \sim -17$ kJ/mol and the magnitude is smaller compared with the ΔE for EtOH (see Figure 5). The reason is that EtOH is bigger in size and contains more atoms than H$_2$O, thus, has a stronger interaction with the linker. Among the five linkers, the ΔE decreases in the order of ZIF-78 > -79 > -69 > -81 > -68. The Q_{st}^o are also shown in Figure 12. The predicted Q_{st}^o in ZIF-68 is about 35.5 kJ/mol, matching well with the experimental result extrapolated to zero loading (34.5 kJ/mol).[26] In the five ZIFs, Q_{st}^o decreases as ZIF-78 > -79 > -69 > -81 > -68, following the trend of ΔE. The nbIm linkers in ZIF-78 exhibits the greatest ΔE due to H-bonding between —NO$_2$ group and H$_2$O, leading to the greatest Q_{st}^o. Compared with parent ZIF-68, the ΔE and Q_{st}^o in ZIF-79, −69, and −81 are greater. As discussed earlier, the functional groups enhance ZIF-H$_2$O interaction and promote adsorption at a low loading.

To elucidate why H$_2$O uptake in ZIF-79 at an intermediate pressure is much lower than in ZIF-68, −69, −78, and −81, Figure 13 illustrates the density distributions in ZIF-79 at 0.001, 4, and 8 kPa. Over a wide range of pressure from 0.001 to 4 kPa, H$_2$O molecules are almost exclusively adsorbed in the small pores and no discernible adsorption is
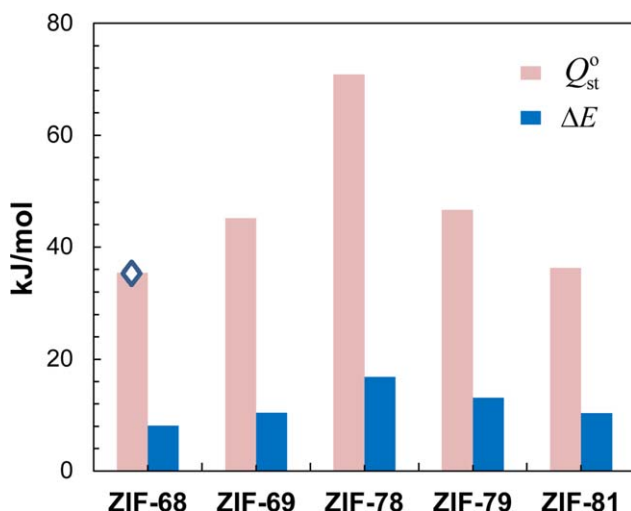
Figure 12. Binding energies between H$_2$O and bIm linkers, and isosteric heats at infinite dilution of H$_2$O in ZIF-68, −69, −78, −79, and −81.

The ◇ indicates experimental result.[26] [Color figure can be viewed in the online issue, which is available at wileyonlinelibrary.com.]
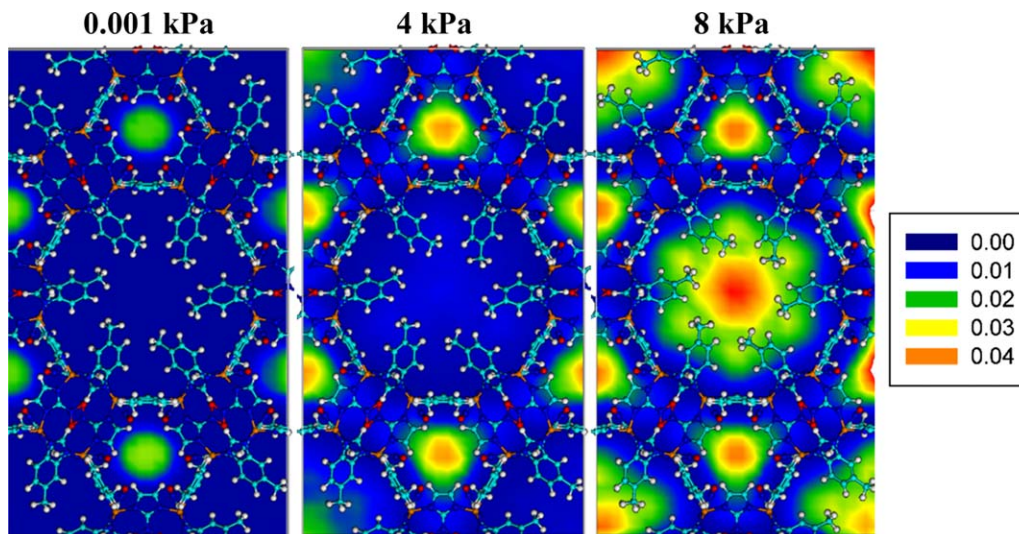
Figure 13. Density contours of H₂O in ZIF-79 at 0.001, 4, and 8 kPa.

The unit of density scale is the number of molecules per Å³. [Color figure can be viewed in the online issue, which is available at wileyonlinelibrary.com.]

observed in the large pores. This is remarkably different from H₂O adsorption in the other four ZIFs, where the large pores are already filled at an intermediate pressure (e.g., 4 kPa). The reason is because the bulky hydrophobic $-CH_3$ groups in ZIF-79 exert a steric hindrance and impede polar H₂O entering the large pores. Only at a high pressure (e.g., 8 kPa), H₂O is able to enter the large pores and exhibits comparable uptake with the other four ZIFs. From this analysis, we can infer that it is of central importance to unambiguously understand adsorption behavior by visualizing simulation snapshots.

EtOH/H₂O mixtures

Here biofuel is mimicked by EtOH/H₂O liquid mixtures. Figure 14 plots the simulated adsorption isotherms in ZIF-68, −69, −78, −79, and −81 at 298 K. The general trend in the five ZIFs is similar. When the composition of EtOH in bulk phase X_{EtOH} is very low, H₂O is more dominantly adsorbed than EtOH. On increasing X_{EtOH}, EtOH uptake increases gradually, while H₂O uptake decreases sharply. The separation performance is quantified by selectivity
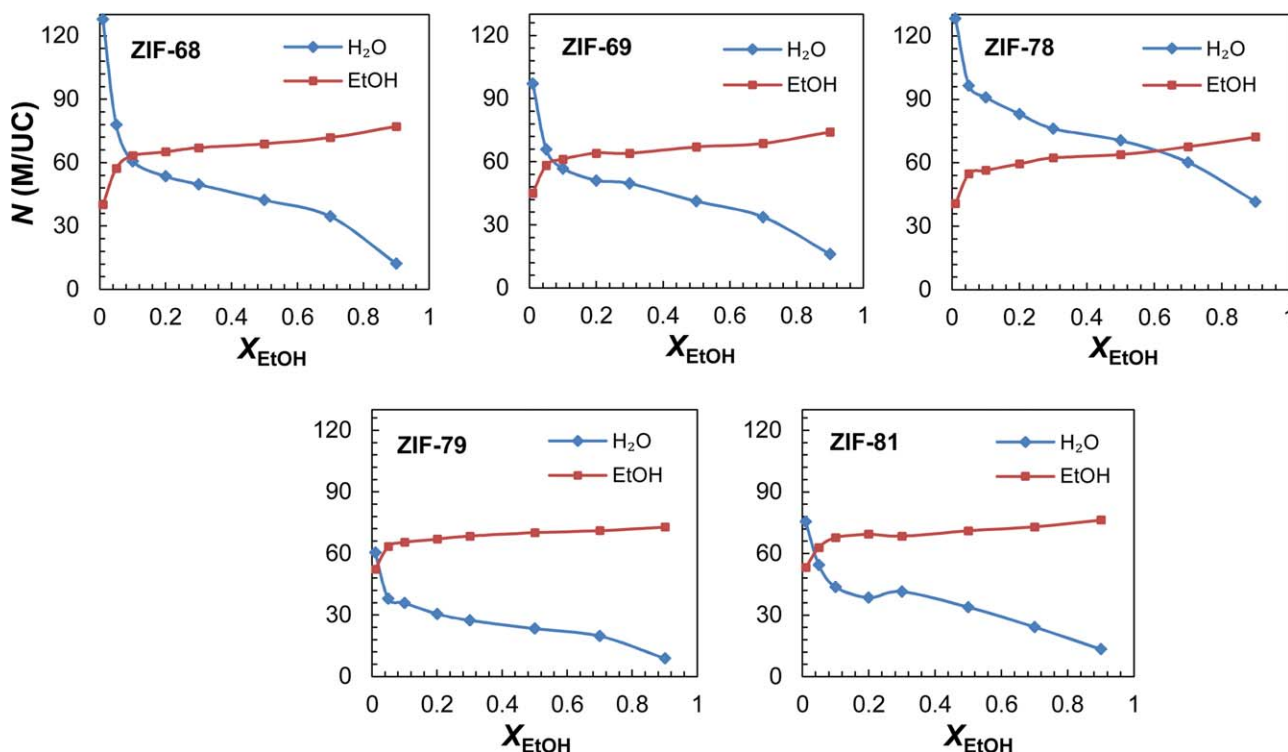
Figure 14. Adsorption isotherms of EtOH/H₂O mixtures at 298 K.

[Color figure can be viewed in the online issue, which is available at wileyonlinelibrary.com.]
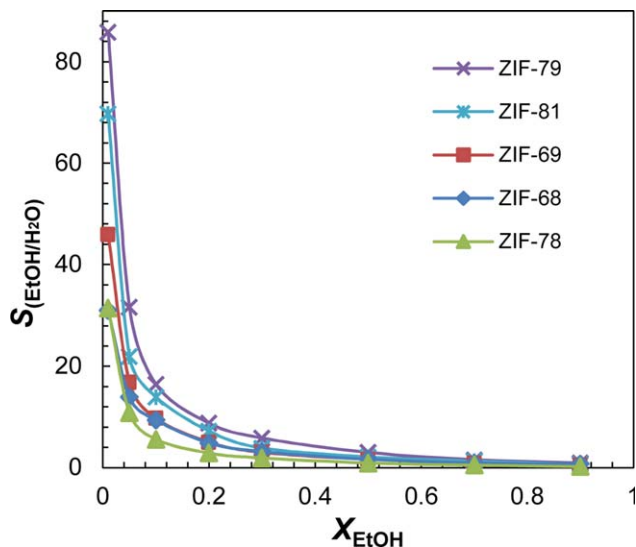
Figure 15. Adsorption selectivities of EtOH/H₂O mixtures at 298 K.

[Color figure can be viewed in the online issue, which is available at wileyonlinelibrary.com.]

$$S_{ad(i/j)} = \left(Y_i / Y_j\right) / \left(X_i / X_j\right) \tag{9}$$

where Y_i and X_i are the compositions of component i in adsorbed and bulk phase, respectively. Figure 15 plots the selectivities of EtOH over H₂O in the five ZIFs. With increasing X_{EtOH}, the selectivity in each ZIF drops. At a given X_{EtOH}, the selectivity decreases as ZIF-79 > -81 > -69 > -68 > -78. ZIF-79 has the highest selectivity, as discussed above, the hydrophobic —CH₃ groups impede H₂O adsorption to the greatest extent compared with the other four ZIFs. Similar but smaller effect is seen in ZIF-81 and −69 consisting of —Br and —Cl groups. Conversely, ZIF-78 exhibits the lowest selectivity due to its hydrophilic nature and the most favorable for H₂O adsorption among the five ZIFs. Biofuel produced via fermentation usually contains a low concentration of EtOH ($X_{EtOH} = 0.01 \sim 0.05$). At $X_{EtOH} = 0.01$, the highest selectivity is approximately 86 in

ZIF-79, which might be a promising candidate for biofuel purification.

As ZIF-79 exhibits the best separation performance among the five ZIFs, the density distributions of EtOH and H₂O in ZIF-79 are plotted in Figure 16. At $X_{EtOH} = 0.05$, EtOH is adsorbed in the small pores and the six corners of the large pores (near —CH₃ groups). Although pure H₂O only resides in the small pores at low and intermediate pressure (Figure 13), H₂O is able to enter the center of the large pores in the presence of EtOH. The reason is that EtOH existing in the large pores can act as seeds and promote H₂O adsorption. This cooperative phenomenon was also observed previously in the adsorption of EtOH/H₂O mixtures in other ZIFs[19] and Zn(bdc)(ted)₀.₅.[48] At $X_{EtOH} = 0.5$, EtOH is more populated in both the small and large pores, and H₂O in the center of the large pores is partially replaced by EtOH. The replacement of H₂O by EtOH is almost complete at $X_{EtOH} = 0.9$ as a consequence of competitive adsorption.

Conclusions

Adsorption of ethanol/water in ZIF-68, −69, −78, −79, and −81 has been investigated by integrating *ab initio* calculations and molecular simulations. While the adsorption isotherms predicted by the three force fields (UFF, DREIDING, and AMBER) match reasonably well with experimentally measured data, the DREIDING appears to outperform over the UFF and AMBER. For ethanol, the isotherms are type I in the five ZIFs; for water, they are type I in ZIF-78 and type V in ZIF-68, −69, −79, and −81. This suggests the favorable interaction for ethanol in the five ZIFs, and ZIF-78 tends to be more hydrophilic than the other four ZIFs. At a low pressure, adsorption is observed to be mainly in the small pores and the six corners of the large pores. The uptakes of ethanol and water decrease as ZIF-78 > -79 > -69 > -81 > -68 and ZIF-78 > -69 > -79 > -81 > -68, respectively. It is obvious that the adsorbate-ZIF interaction is enhanced by the functionalization of bIm linkers in ZIF-68. Particularly, the large number of —NO₂ groups of nbIm linkers in ZIF-78 can form strong hydrogen-bonding with ethanol or water, and thus, the largest enhancement is observed in ZIF-78. The isosteric heats at
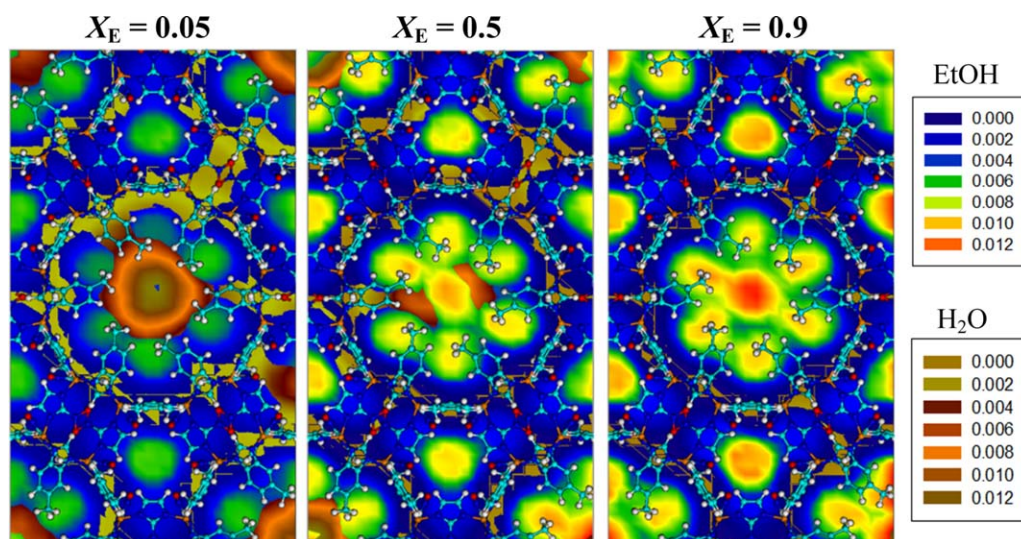
Figure 16. Density contours of EtOH/H₂O mixtures in ZIF-79 at 298 K.

The unit of density scale is the number of molecules per Å³. [Color figure can be viewed in the online issue, which is available at wileyonlinelibrary.com.]

infinite dilution closely follow the trend of uptakes, and are consistent with the binding energies between adsorbates and substituted bIm linkers. At a high pressure, pore-filling occurs in the large pores; thus, the uptakes are primarily proportional to free volume, although also affected by H-bonding particularly in ZIF-78. The mobility of adsorbate near saturation condition follows the hierarchy of free volume. In ZIF-68 with the largest free volume, the mobility is the highest; and vice versa in ZIF-79. For ethanol/water mixtures mimicking biofuel, the selectivities in the five ZIFs decrease with increasing composition of ethanol. Due to its hydrophilic feature, ZIF-78 has the lowest selectivity. In contrast, ZIF-79 is the most hydrophobic among the five ZIFs and exhibits the highest selectivity, around 86 at the ethanol composition of 0.01. This suggests that ZIF-79 might be interesting for ethanol/water separation. These bottom-up insights are useful for the further development of new ZIFs and other nanoporous materials for high-performance biofuel purification.

Acknowledgments

Literature Cited

1. Keith DW. Why capture CO_2 from the atmosphere? *Science*. 2009; 325:1654–1655.
2. Schubert C. Making fuels for the future. *Nature*. 2011;474:531–533.
3. Koonin SE. Getting serious about biofuels. *Science*. 2006;311:435–436.
4. *Agricultural Outlook 2010–2019*, Food and Agriculture Organization of the United Nations.
5. Antoni D, Zverlov VV, Schwarz WH. Biofuels from microbes. *Appl Microbiol Biotechnol*. 2007;77:23–35.
6. Garcia M, Sanz MT, Beltran S. Separation by pervaporation of ethanol from aqueous solutions and effect of other components present in fermentation broths. *J Chem Technol Biotechnol*. 2009;84:1873–1882.
7. Venkatesan S. Adsorption. In: *Separation and Purification Technologies in Biorefineries*. West Sussex: Wiley, 2013:101–148.
8. Jones RA, Tezel FH, Thibault J, Tolan JS. Bioethanol production to be blended with gasoline: improvements in energy use by adsorption. *Int J Enery Res*. 2007;31:1517–1531.
9. Oudshoorn A, van der Wielen LAM, Straathof AJJ. Adsorption equilibria of bio-based butanol solutions using zeolite. *Biochem Eng J*. 2009;48:99–103.
10. Yaghi OM, O'Keefe M, Ockwig NW, Chae HK, Eddaoudi M, Kim J. Reticular synthesis and the design of new materials. *Nature*. 2003; 423:705–714.
11. Furukawa H, Cordova KE, O'Keeffe M, Yaghi OM. The chemistry and applications of metal-organic frameworks. *Science*. 2013;341: 1230444.
12. Suh MP, Park HJ, Prasad TK, Lim DW. Hydrogen storage in metal-organic frameworks. *Chem Rev*. 2012;112:782–835.
13. Sumida K, Rogow DL, Mason JA, McDonald TM, Block ED, Herm ZR, Bae TH, Long JR. Carbon dioxide capture in metal-organic frameworks. *Chem Rev*. 2012;112:724–781.
14. Li JR, Sculley J, Zhou HC. Metal-organic frameworks for separations. *Chem Rev*. 2012;112:869–932.
15. Saint Remi JC, Rémy T, Van Hunskerken V, van de Perre S, Duerinck T, Maes M, De Vos D, Gobechiya E, Kirschhock CEA, Baron GV, Denayer JFM. Biobutanol separation with the metal–organic framework ZIF-8. *ChemSusChem*. 2011;4:1074–1077.
16. Zhang K, Lively RP, Dose ME, Brown AJ, Zhang C, Chung J, Nair S, Koros WJ, Chance RR. Alcohol and water adsorption in zeolitic imidazolate frameworks. *Chem Commun*. 2013;49:3245–3247.
17. Zhang K, Lively RP, Zhang C, Koros WJ, Chance RR. Investigating the intrinsic ethanol/water separation capability of ZIF-8: an adsorption and diffusion study. *J Phys Chem C*. 2013;117:7214–7225.
18. Nalaparaju A, Zhao XS, Jiang JW. Biofuel purification by pervaporation and vapor permeation in metal–organic frameworks: a computational study. *Energy Environ Sci*. 2011;4:2107–2116.
19. Zhang K, Nalaparaju A, Chen YF, Jiang JW. Biofuel purification in zeolitic imidazolate frameworks: the significant role of functional groups. *Phys Chem Chem Phys*. 2014;16:9643–9655.
20. Banerjee R, Furukawa H, Britt D, Knobler C, O'Keeffe M, Yaghi OM. Control of pore size and functionality in isoreticular zeolitic imidazolate frameworks and their carbon dioxide selective capture properties. *J Am Chem Soc*. 2009;131:3875–3877.
21. Banerjee R, Phan A, Wang B, Knobler C, Furukawa H, O'Keeffe M, Yaghi OM. High-throughput synthesis of zeolitic imidazolate frameworks and application to CO_2 capture. *Science*. 2008;319: 939–943.
22. Smart OS, Neduvelil JG, Wang X, Wallace BA, Sansom MSP. Hole: a program for the analysis of the pore dimensions of ion channel structural models. *J Mol Graphics*. 1996;14:354–360.
23. Düren T, Millange F, Ferey G, Walton KS, Snurr RQ. Calculating geometric surface areas as a characterization tool for metal-organic frameworks. *J Phys Chem C*. 2007;111:15350–15356.
24. Babarao R, Hu ZQ, Jiang JW, Chempath S, Sandler SI. Storage and separation of CO_2 and CH_4 in silicalite, C_{168} schwarzite, and IRMOF-1: a comparative study from monte carlo simulation. *Langmuir*. 2007;23:659–666.
25. Van der Perre S, Van Assche T, Bozbiyik B, Lannoeye J, De Vos DE, Baron GV, Denayer JFM. Adsorptive characterization of ZIF-68: a complex structure with amphiphilic properties. *Langmuir*. 2014;30:8416–8424.
26. Van der Perre S, Bozbiyik B, Lannoeye J, De Vos DE, Baron GV, Denayer JFM. Experimental study of adsorptive interactions of polar and non-polar adsorbates in ZIF-68 via pulse gas chromatography. *J Phys Chem C*. 2015;119:1832–1839.
27. Zhang C, Lively RP, Zhang K, Johnson JR, Karvan O, Koros WJ. Unexpected molecular sieving properties of zeolitic imidazolate framework-8. *J Phys Chem Lett*. 2012;3 2130–2134.
28. Zhang K, Lively RP, Zhang C, Chance RR, Koros WJ, Sholl DS, Nair S. Exploring the framework hydrophobicity and flexibility of ZIF-8 from biofuel recovery to hydrocarbon separations. *J Phys Chem Lett*. 2013;4:3618–3622.
29. Mayo SL, Olafson BD, Goddard WA. DREIDING, a generic force-field for molecular simulations. *J Phys Chem*. 1990;94:8897–8909.
30. Rappe AK, Casewit CJ, Colwell KS, Goddard WA, Skiff WM. UFF, a full periodic-table force-field for molecular mechanics and molecular dynamics simulations. *J Am Chem Soc*. 1992;114:10024–10035.
31. Duan Y, Wu C, Chowdhury S, Lee MC, Xiong GM, Zhang W, Yang R, Cieplak P, Luo R, Lee T, Caldwell J, Wang JM, Kollman P. A point-charge force field for molecular mechanics simulations of proteins based on condensed-phase quantum mechanical calculations. *J Comput Chem*. 2003;24:1999–2012.
32. Frisch MJ, Trucks GW, Schlegel HB, Scuseria GE, Robb MA, Cheeseman JR, Zakrzewski VG, Montgomery JA, Stratmann RE, Burant JC, Dapprich S, Millam JM, Daniels AD, Kudin KN, Strain MC, Farkas O, Tomasi J, Barone V, Cossi M, Cammi R, Mennucci B, Pomelli C, Adamo C, Clifford S, Ochterski J, Petersson GA, Ayala PY, Cui Q, Morokuma K, Malick DK, Rabuck AD, Raghavachari K, Foresman JB, Cioslowski J, Ortiz JV, Stefanov BB, Liu G, Liashenko A, Piskorz P, Komaromi I, Gomperts R, Martin RL, Fox DJ, Keith T, Al-Laham MA, Peng CY, Nanayakkara A, Gonzalez C, Challacombe M, Gill PMW, Johnson BG, Chen W, Wong MW, Andres JL, Head-Gordon M, Replogle ES, Pople JA. *Gaussian 09*, Revision D.01, Wallingford CT: Gaussian Inc., 2009.
33. Chen B, Potoff JJ, Siepmann JI. Monte carlo calculations for alcohols and their mixtures with alkanes. transferable potentials for phase equilibria. 5. united-atom description of primary, secondary, and tertiary alcohols. *J Phys Chem B*. 2001;105:3093–3104.
34. Jorgensen WL, Chandrasekhar J, Madura JD, Impey RW, Klein ML. Comparison of simple potential functions for simulating liquid water. *J Chem Phys*. 1983;79:926–935.
35. Boys SF, Bernardi F. The calculations of small molecular interaction by the difference of separate total energies-some procedures with reduced error. *Mol Phys*. 1970;19:563–566.
36. Frenkel D, Smit B *Understanding Molecular Simulation: From Algorithms to Applications*. San Diego, Academic Press, 2002.
37. Zhang K, Zhang LL, Jiang JW. Adsorption of C_1–C_4 alcohols in zeolitic imidazolate framework-8: effects of force fields, atomic charges, and framework flexibility. *J Phys Chem C*. 2013;117: 25628–25635.
38. Gee JA, Chung J, Nair S, Sholl DS. Adsorption and diffusion of small alcohols in zeolitic imidazolate frameworks ZIF-8 and ZIF-90. *J Phys Chem C*. 2013;117:3169–3176.

39. Visco DP Jr, Kofke DA. Modeling the monte carlo simulation of associating fluids. *J Chem Phys*. 1999;110:5493–5502.
40. Vlugt TJH, Smit B. BIGMAC. http://molsim.chem.uva.nl/bigmac/. 1998.
41. Van Der Spoel D, Lindahl E, Hess B, Groenhof G, Mark AE, Berendsen HJC. Gromacs: fast, flexible, and free. *J Comput Chem*. 2005;26:1701–1718.
42. Linstrom PJ, Mallard WG. NIST Chemistry WebBook. http://webbook.nist.gov/chemistry/. *U.S. Secretary of Commerce*, 2011.
43. Goncalves RM. The enthalpy and entropy of cavity formation in liquids and corresponding states principle. *Can J Chem*. 1990;68: 1937–1949.
44. Fan L, Xue M, Kang Z, Wei G, Huang L, Shang J, Zhang D, Qiu S. ZIF-78 membrane derived from amorphous precursors with permselectivity for cyclohexanone/cyclohexanol mixture. *Microporous Mesoporous Mater*. 2014;192:29–34.
45. Castillo JM, Vlugt TJH, Calero S. Understanding water adsorption in Cu-BTC. *J Phys Chem C*. 2008;112:15934–15939.
46. De Lange MF, Gutierrez-Sevillan JJ, Hamad S, Vlugt TJH, Calero S, Gascon J, Kapteijn F. Understanding adsorption of highly polar vapors on mesoporous MIL-100 and MIL-101: experiments and molecular simulations. *J Phys Chem C*. 2013; 117:7613−7622.
47. Ghosh P, Kim KC, Snurr RQ. Modeling water and ammonia adsorption in hydrophobic metal−organic frameworks: single components and mixtures. *J Phys Chem C*. 2014;118:1102–1110.
48. Chen YF, Lee JY, Babarao R, Li J, Jiang JW. A highly hydrophobic metal-organic framework $Zn(bdc)(ted)_{0.5}$ for adsorption and separation of CH_3OH/H_2O and CO_2/CH_4: an integrated experimental and simulation study. *J Phys Chem C*. 2010;114: 6602–6609.